

See discussions, stats, and author profiles for this publication at: <https://www.researchgate.net/publication/221695318>

# Insight into the 3D Architecture and Quasicrystal Symmetry of Multilayer Nanorod Assemblies from Moire Interference Patterns

ARTICLE *in* ACS NANO · MARCH 2012

Impact Factor: 12.88 · DOI: 10.1021/nn300331x · Source: PubMed

---

CITATIONS

26

---

READS

27

## 3 AUTHORS, INCLUDING:



Ajay Singh

Lawrence Berkeley National Laboratory

34 PUBLICATIONS 617 CITATIONS

SEE PROFILE

# Insight into the 3D Architecture and Quasicrystal Symmetry of Multilayer Nanorod Assemblies from Moiré Interference Patterns

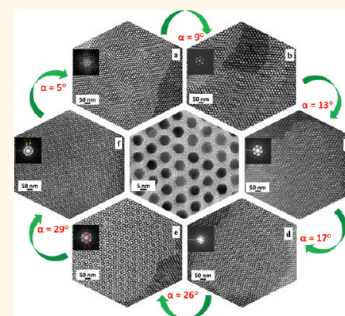
Ajay Singh,<sup>†,‡</sup> Calum Dickinson,<sup>†</sup> and Kevin M. Ryan<sup>†,‡,\*</sup>

<sup>†</sup>Materials and Surface Science Institute and Department of Chemical and Environmental Sciences, University of Limerick, Limerick, Ireland and <sup>‡</sup>SFI-Strategic Research Cluster in Solar Energy Research, University of Limerick, Limerick, Ireland

Moiré interference patterns occur when two lattices overlap with a rotational misorientation and are independent of length scale once the effect is observable to the eye.<sup>1</sup> These patterns, initially only of aesthetic interest, are now finding important applications for characterizing the three-dimensional architecture of layered nanomaterials.<sup>2,3</sup> As these materials can be imaged in transmission mode (TEM, STEM, or STM), sequential layers that have an angular offset generate Moiré patterns in the upscaled images, allowing three-dimensional structural determination in both crystalline (e.g., anodic alumina)<sup>4</sup> and noncrystalline materials (e.g., self-patterned block copolymers).<sup>5</sup> In samples of the important electronic material graphene, Moiré patterns allow nondestructive characterization of whether the desired monolayer or multilayer is present.<sup>6–8</sup> Equally, Moiré patterns in folded biological cell membranes allow the structural biology arising from lipid packing to be elucidated.<sup>9</sup> The pattern formation not only is a powerful tool for the three-dimensional characterization of layered materials with nanoscale order but is expected to find application in complex lithographic patterning.<sup>4</sup>

Moiré patterns have particular importance in the area of nanocrystal assembly, as the interparticle length scales (1–10 nm) allow manifestation of interference patterns that allow detailed interpretation of the three-dimensional structure.<sup>10–19</sup> As new materials with extraordinary properties are designed with nanocrystal size, elemental composition (metal, semiconductor), heteroparticulate distribution, and interparticle spacing as control factors, techniques that reveal the precise three-dimensional architecture are

**ABSTRACT** Vertical nanorod assembly over three dimensions is shown to result in the formation of Moiré interference patterns arising from rotational offsets between respective monolayer sheets. Six distinct patterns are observed in HRTEM and angular dark-field STEM (DF-STEM) images, allowing the exact angle of rotation to be determined from their respective size and repeat order. At large rotation angles approaching 30°, the aperiodicity in the structure of the nanorod supercrystals becomes apparent, resulting in 12-fold ordering characteristics of a quasicrystal. The rotational offsets are further elucidated from Fourier transform and small angle electron diffraction, allowing interpretation of several multilayers when combined with DF-STEM and SEM. Pattern formation owing to angular rotation is differentiated from those occurring from a lateral shift, providing an important insight into the complex multilayered structures in assembled rods that may have an impact on their collective electronic or photonic properties. We also show how random tetrapods when present at low concentrations in colloidal nanorod solutions act as termination points for 2D sheet crystallization, impacting the size and shape of the resultant assemblies. The occurrence of Moiré patterns in rod assemblies demonstrates the extraordinary order achievable in their assembly and offers a nondestructive technique to precisely map the placement of each nanorod in this important nanoarchitecture.



**KEYWORDS:** nanocrystal · nanorod · perpendicular assembly · Moiré pattern · tetrapod · DF-STEM

of critical importance.<sup>10–23</sup> As spherical nanocrystals arrange in expected packing parameters as a function of radius, Moiré patterns have been observed and used to elucidate the simplest AB binary superlattice through to structures with forbidden symmetry (quasicrystals).<sup>10–15</sup> In colloidal nanocrystals, the further ability to control shape<sup>24–26</sup> adds even greater complexity to possible superstructure formation.<sup>27</sup> Recent advances in nanorod assembly, using self-directed or

\* Address correspondence to kevin.m.ryan@ul.ie.

Received for review January 23, 2012 and accepted March 12, 2012.

Published online March 12, 2012  
10.1021/nn300331x

© 2012 American Chemical Society

directed methodologies, have allowed large-scale architectures to be formed where each rod is vertically aligned and close packed.<sup>27–40</sup> In this geometry, the collective absorption or luminescence of the oriented rods can be optimized by tuning the length while retaining size-defined properties dependent on the diameter, such as band gap.<sup>41,42</sup> These superstructures have outstanding promise with emergent applications impacting energy conversion (photovoltaics and photocatalysis), electronics (semiconductor patterning), and photonics (subdiffraction wave guides) in development.<sup>42–44</sup> The principle challenge being addressed is extending the assembly size to meaningful scales where the nature of assembly (either 1D or 2D) and number of assembled layers can be controlled.<sup>34,35</sup> The subsequent and equally important challenge will be in characterizing these 3D architectures such that the precise position and placement of each nanorod building block is known.

Here we report the formation of an array of complex Moiré interference patterns from self-assembled nanorods, demonstrating the extraordinary order attainable with these materials. The Moiré patterns are uniquely characterized by angular dark-field STEM (DF-STEM) and referenced against SAED, HRTEM, and HRSEM for comparison. Six distinct patterns are observed and are indexed to an angular rotation between underlying sheets, allowing the three-dimensional architecture to be accurately determined. The interpretation of additional lateral stacking faults and defects owing to random tetrapod distribution offers a critical depth of understanding necessary for next-generation applications incorporating orthogonal rod assembly.

## RESULTS AND DISCUSSION

Colloidal II–VI nanorods have a permanent dipole moment and a net charge that varies, primarily as a function of ligand.<sup>45,46</sup> We have recently shown that the simplest method to achieve a perpendicular assembly in solution is to direct the total energy considerations such that attractive interactions (dipole–dipole) slightly outweigh repulsive interactions (Coulombic) to allow supercrystallization.<sup>34,35</sup> Nucleation of assembly thereby has a distance and hence concentration dependence that when suboptimal will result in random rod alignment, as highlighted in Figure 1a, and when optimized allows formation of a perfect 2D supercrystal layer (see Supporting Information, Figure S1) that forms on the surface after sedimentation from solution. Apart from a prerequisite tight size distribution in both length and diameter of the rods, here ( $7 \times 30$  nm), this method of assembly requires no external directing agents or addition of additives, resulting in a defect-free assembly with minimal contamination from excess organics (Figure 1b). The 2D sheets can be deposited sequentially, forming multilayer arrays, as shown in the SEM image in Figure 1c, when the rate of

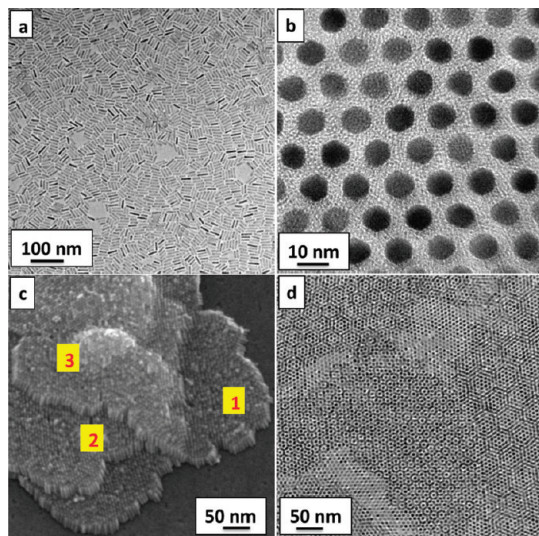


**Figure 1.** (a) TEM image showing randomly lying CdS nanorods ( $7 \times 30$  nm). (b) HRTEM showing top-down image of vertically oriented close-packed CdS nanorods. (c) SEM image showing the multilayer, vertical assembly of nanorod superstructures. (d) TEM image showing different Moiré patterns revealed in CdS nanorod superstructures.

evaporation of the solvent is controlled. The rods at the edges of each layer are perfectly orthogonal, confirming that each layer forms as a preassembled sheet in solution. Imaging these multilayer assemblies in transmission mode (TEM, STEM) results in characteristic Moiré interference patterns, Figure 1d (Figure S2), that vary depending on the number of monolayers.

Scanning transmission electron microscopy (STEM) removes the diffraction contrast commonly seen in the TEM images, leaving only the mass thickness contrast. As the rods have a larger mass than the carbon support film, and are of similar mass and thickness, the only contrast difference in DF-STEM results from overlapped layers. Figure 2 shows the range of different Moiré patterns seen in the DF-STEM images of multi-layered CdS hexagonal sheets. Each image consists of a first (base) layer and a second layer, with the difference between each image occurring due to a rotational offset between each layer. The interference pattern reveals itself initially as a repeating hexagonal motif the size of which correlates with a specific angle of rotation between underlying sheets (Supporting Information, Figure S3). This is highlighted with  $5^\circ$  rotation (Figure 2a), resulting in a center-to-center distance of 116 nm, sequentially decreasing with larger angular rotations of  $9^\circ$ ,  $13^\circ$ , and  $17^\circ$  in Figure 2b–d, respectively. The inverse relationship between the angle of rotation and size of the motif is expected, as lines or patterns appear only when the cumulative effect of the rotational offset is sufficient to reveal a distinct image of a row of rods in an underlying layer. The measured motif repeat distance ( $D_{\text{motif}}$ ) for each rotation angle,  $\alpha$ , is in good agreement with the theoretical value  $D_{\text{rm}}$  obtained from the rotational Moiré equation

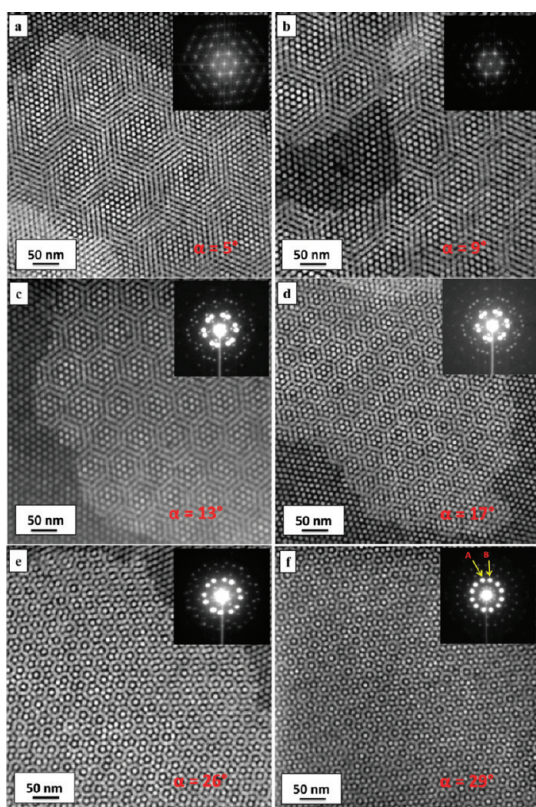


**Figure 2.** (a–e) DF-STEM images and the corresponding FFT and SAED patterns (inset) of Moiré patterns arising from the stacking of two sheets of vertically oriented CdS nanorod superlattice films. Misorientation angle: (a)  $\sim 5^\circ$ , (b)  $\sim 9^\circ$ , (c)  $\sim 13^\circ$ , (d)  $\sim 17^\circ$ , (e)  $\sim 26^\circ$ . (f) DF-STEM image with inset SAED pattern showing a 12-fold quasicrystalline-like Moiré pattern that is revealed when the misorientation angle between two CdS nanorod layers is close to  $30^\circ$ .

(Supporting Information, Table S4).<sup>1</sup> Rotational Moiré patterns from offsets as small as  $1^\circ$  are observable, as the repeat motifs are in the submicrometer range (570 nm) and are hence smaller than the typical assembly dimensions (additional DF-STEM images of Moiré patterns observed for other misorientation angles are shown in Supporting Information, Figure S5).

As the rotation angles increase to  $>17^\circ$ , the size of the motif decreases and the aperiodic symmetry of the motifs is revealed. When the misorientation angle approaches  $30^\circ$ , pattern symmetry resembles the traditional 12-fold ordering seen in quasicrystals.<sup>10</sup> Here the quasicrystal in nanorod superstructures lack translational symmetry but possess rotational symmetry originating from the directionality of the nanorod superstructure. This resemblance to quasicrystals occurs as when one ordered sheet settles randomly on top of another ordered sheet, the resulting Moiré pattern cannot be entirely disordered and should instead be aperiodic. If one or both sheets have a small amount of disorder, then this aperiodic structure is less well formed. The hexagonal symmetry in the nanorods means that each  $30^\circ$  rotation is equivalent to  $0^\circ$  rotation such that  $45^\circ$  corresponds to a  $15^\circ$  Moiré

pattern. The importance of the uniform size and shape of the rods becomes apparent in these patterns when perfectly columnar CdS rods are compared to “rice-shaped” CdSe rods, where a 10% pinhole vacancy causes the aperiodicity to be disrupted and no long-range ordering can be seen (Supporting Information, Figure S6).

The fast Fourier transforms (FFTs) and small-angle electron diffraction (SAED) are a result of the individual hexagonal diffraction of each overlapping layer (given as A and B). A large camera length (200 cm) was used for the SAED to get information only from the hexagonal ordering and not the crystal structure. Measuring the angle between the spots from two patterns results in the calculation of the misorientation angle. The low angle spots up to  $10^\circ$  manifests as a broadening in the low index peaks, and separate spots for the two layers become apparent only in the second or third rings. As a result FFTs are normally best used for the low angles due to the intensities and proximity of the two spots (Figure 2a and b insets). The separate spots for A and B layers can be more clearly seen in Figure 2c and d, where the misorientation angle is increased. As the angles increase, the two spots diverge further, tending toward a 12-fold quasicrystal as the rotation approaches  $30^\circ$ .

Interestingly, the diffraction patterns and FFTs are not purely two separate diffraction patterns overlapped, like that commonly seen for twin defects. Instead, there is the presence of satellite spots coming from the Moiré superstructure from the overlapped layers. This is due to the multiplication of intensities, leading to the convolution of diffraction patterns in which the frequency vectors are added vectorially, while the corresponding impulse amplitudes are multiplied.<sup>1,5</sup> As a result, these satellite spots cannot be indexed using the standard Miller indexing ( $hkl$ ) and as a result need a minimum of two extra vectors added. This indexing and explanation are given in the Supporting Information (Figure S7). Figure 2f and the inset SAED image clearly show this unique symmetry found in the nanorod superlattice and is in good agreement with the previous report<sup>5,10,12</sup> (larger images of SAED for all rotation angles can be seen in Supporting Information, Figure S8).

Moiré patterns also form when more than two sheets overlap but are more complex due to the sum of rotational differences, although indexing is possible. Figure 3 a shows an example of this multilayer, with the three sheets easily identifiable in the DF-STEM image. M1,2 and M1,3 are first-order Moiré patterns, with  $9^\circ$  and  $26^\circ$  misorientation, respectively, and M1,2,3 is a second-order Moiré pattern, which is made up from all three layers. As above, the misorientation angle can be calculated from the first-order Moiré patterns (M1,2 and M1,3) either from the size of the hexagonal motifs or from FFT. M1,2,3 as a second-order Moiré pattern, however, cannot be determined from

the image alone; therefore FFT or SAED needs to be employed. An FFT on each region M1,2 and M1,3 reveals two misoriented hexagonal patterns corresponding to rotational misorientations of  $9^\circ$  and  $26^\circ$ , respectively, as expected. Three misoriented hexagonal patterns can be identified from the FFT M1,2,3, correlating with the number of layers. Comparison of this pattern with the corresponding FFTs of M1,2 and M1,3 allows the degree of misorientation between the hidden layers M2,3 to be identified as  $17^\circ$  (additional DF-STEM images of Moiré patterns in multilayer nanorod superlattices and FFTs are in Supporting Information, Figure S9).

An absence of Moiré patterns occurs when either there is no rotation or the offset is at exact multiples of

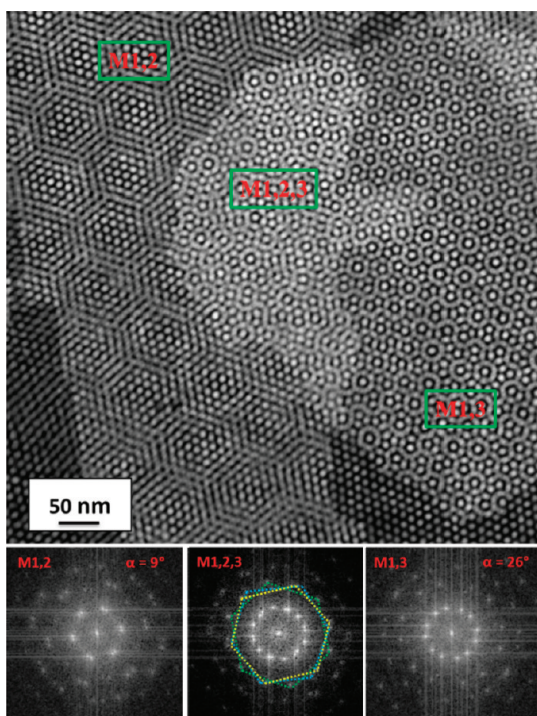


**Figure 3.** First-order (M1,2 and M1,3) and second-order Moiré patterns (M1,2,3) in the DF-STEM image and FFT pattern of each respective area.

$30^\circ$  (Figure 4a). However different pattern formation occurs in Figure 4b, where there is no rotational offset but a lateral shift occurs. The hexagonal structure of the layers can still be seen to be intact (FFT inset of Figure 4b with no first-order Moiré patterns present). Figure 4c is a higher resolution image of Figure 4b; the yellow indicates the first layer and the green the second layer. This shift of  $\sim 1/3$  of the unit cell can easily be seen due to the visibility of the space between the rods forming a hexagonal pattern. Other fractional shifts are of course possible and are quite often difficult to distinguish from tilted hexagonal sheets (Supporting Information, Figure S10).

A noticeable feature of the 2D monolayer sheets of CdS nanorods is their termination with apparently random angular edges. Closer examination Figure 5a, b reveals the presence of tetrahedral-shaped nanocrystals (tetrapods) that act to terminate the growth of the supercrystal. Tetrapods form as a percentage of each colloidal synthesis due to nucleation of some

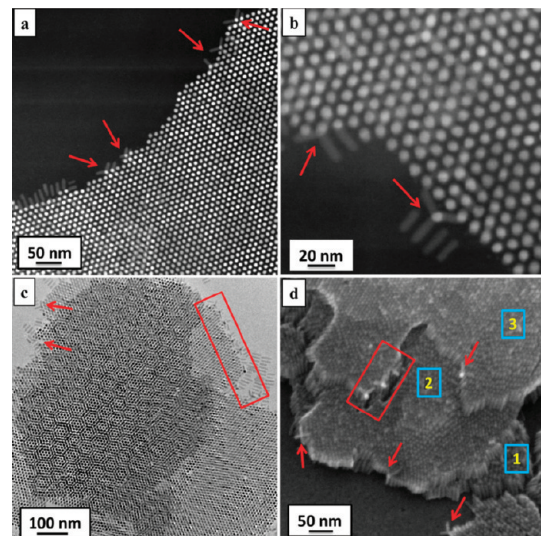


**Figure 5.** (a–c) DF-STEM and TEM show the presence of single and multiple tetrapods in a nanorod assembly. (d) SEM image revealing the presence of a tetrapod in the second and third layer of CdS nanorod superstructures.

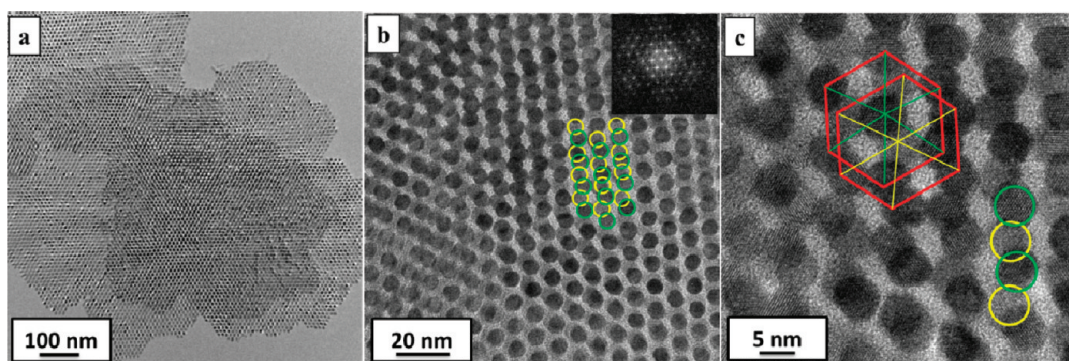


**Figure 4.** (a) TEM image showing no Moiré pattern generated when two 2D sheets overlap perfectly ( $0^\circ$  misorientation angle). (b, c) TEM and HRTEM images clearly indicate the lateral shifts between two 2D sheets, respectively. The inset FFT in (b) shows only one hexagonal pattern.

crystals in the zinc-blende instead of wurtzite phase, and while they can be reduced through growth control, their complete elimination is difficult to achieve.<sup>24</sup> The four equivalent length arms are typically of the same dimensions as the colloidal rods, and as such, one arm of the tetrapod can join the supercrystallization with the other three arms acting as a barrier to further addition. Straighter edges of the sheets, such as that from the highlighted region of Figure 5c, reveal multiple tetrapods present in a small area. In multilayers, tetrapods are difficult to distinguish in TEM (Figure 5c) but can be more clearly observed in HRSEM (Figure 5d).

## CONCLUSIONS

The occurrence of Moiré patterns in assembled sheets of vertically aligned semiconductor nanorods not only demonstrates the extraordinary order attainable in their assembly but allows the three-dimensional architecture to be elucidated with precision. The use of STEM as a characterization tool for Moiré patterns

in nanorod assemblies allows detailed contrast resolution and accurate determination of angular rotation between respective monolayer sheets. Coupling the imaging analysis with either Fourier transform or small-angle electron diffraction elucidates the rotational offsets from 1° to 30°. The manifestation of 12-fold quasicrystal symmetry at close to 30° demonstrates that the overlapping sheets are aperiodic in nature. This depth of analysis of multilayer nanorod assemblies reveals the additional patterns related to lateral shifting with no rotation, the interpretation of pattern formation in three or more layers, and the heretofore unobserved influence of tetrapods on rod supercrystallization. The interpretation is generally applicable to understanding and characterizing all nanorod assemblies irrespective of the nature of the material (metal or semiconductor). This insight is particularly consequential and relevant given the rapidly expanding technological advances emerging from these solution-derived nanomaterials.

## METHODS

**Materials.** Cadmium oxide (>99%), trioctylphosphine (TOP, 90%), tri-n-octylphosphine oxide (TOPO, 99%), and sulfur (99.98%) were purchased from Aldrich. n-Octadecylphosphonic acid (ODPA) was obtained from PolyCarbon Industries, Inc. All the chemicals were used as received.

**Synthesis of CdS Nanorods.** In a typical synthesis, 0.20 g of CdO, 1.07 g of ODPA, and 2.74 g of TOPO were loaded into a 25 mL three-neck round-bottom flask, fitted with a reflux condenser and a rubber septum.<sup>25</sup> The mixture in the flask was heated to 100 °C under argon gas until the reactants dissolved. The flask was then evacuated at 100 °C for one hour to remove any excess moisture. The mixture was then heated to 300 °C under Ar gas, whereupon the CdO completely dissolved and the solution became optically clear. The mixture was cooled to 100 °C and further degassed for another 30 min. After this second degassing, the apparatus was switched back to the argon line and the mixture was heated to 300 °C. A 0.8 g sample of sulfur stock solution (0.65 g of sulfur powder dissolved in 8.25 g of TOP) was injected into the flask. After injection, nanocrystals grew at 300 °C for 30 min to reach the desired size. The nanorods were washed 3–5 times to remove excess surfactant by dispersing it in a 1:1 ratio of acetone to toluene. The solution was then centrifuged at 3000 rpm for 3 min, and the sediment was decanted from the supernatant. After all washing, the stock solution of CdS nanorods in toluene was stored in a nitrogen-filled glovebox.

**Formation of Vertically Aligned Close-Packed CdS Nanorod Superstructures.** The nanorod solutions were subjected to repeat (2–3 times) size-selective centrifugation (toluene only) (1000–2000 rpm/3 min) prior to assembly. This allows focusing of the rod size disparity and allows removal of the majority of the tetrapods. The optimum concentration for vertical assembly was determined by drop-casting 7 μL solutions (Eppendorf pipette) of concentrations varying from  $9 \times 10^{-7}$  to  $1 \times 10^{-6}$  mol L<sup>-1</sup> onto a carbon-supported Cu-TEM grid. The solvent was allowed to evaporate slowly in an argon glovebox, with 0% relative humidity, giving a constant evaporation rate (typically 7–10 min total). Rapid evaporation rates of 2–3 min resulted in no observable vertical alignment, with slower rates not changing the degree of alignment but increasing the number of assembled layers depositing on top of each other. The optimum concentration for perfect vertical assembly was found to be  $2.1 \times 10^{-6}$  mol L<sup>-1</sup>. This is the typical process used for the nanorod

assembly formation shown in Figures 1–4. To study the effect of the tetrapods (Figure 5), as-synthesized nanorod solutions containing tetrapods were used without size-selective centrifugation.

**Characterization.** For STEM and TEM analysis, a toluene solution with optimum nanorod concentration was deposited on carbon-supported TEM grids. STEM and TEM images and SAED were obtained using a JEOL JEM-2100F operating at an accelerating voltage of 200 kV. Scanning electron microscopy (SEM) of the nanorod assemblies on a Si(111) substrate was performed with a Hitachi SU-70.

**Conflict of Interest:** The authors declare no competing financial interest.

**Acknowledgment.** This work was supported by Science Foundation Ireland (SFI) under the Principal Investigator Program under contract no. 06/IN.1/I85, 11PI-1148 and also by the Advanced Biomimetic Materials for Solar Energy Conversion Strategic Research Cluster (contract no. 07/SRC/B1160). This work was also conducted under the framework of the INSPIRE Programme, funded by the Irish Government's Programme for Research in Third Level Institutions, Cycle 4, National Development Plan 2007–2013.

**Supporting Information Available:** TEM and STEM images of a monolayer of vertically oriented close-packed CdS nanorods, STEM image showing the multilayer, vertical assembly of nanorod superstructures, schematic representation of a Moiré pattern formed by superposition of two hexagon patterns with a 9° rotation angle, table comparing the measured motif repeat distance ( $D_{\text{motif}}$ ), the rotation angle, and the theoretical value  $D_{\text{rm}}$  obtained from the rotational Moiré equation. Additional DF-STEM image of a Moiré pattern from rice-shaped CdSe rods. Indexed SAED pattern from a Moiré pattern occurring from two overlapping sheets with 26° rotation. FFTs and SAED for all six different Moiré patterns. DF-STEM images and associated FFTs of a CdS superlattice consisting of three layers. Schematic representation of the superposition of two hexagon patterns with ~1/4 lateral shift. This material is available free of charge via the Internet at <http://pubs.acs.org>.

## REFERENCES AND NOTES

1. Amidror, I. *The Theory of the Moiré Phenomenon*; Kluwer Academic Publisher: Norwell, MA, 2000.

2. Kuwabara, M.; Clarke, D. R.; Smith, D. A. Anomalous Super-periodicity in Scanning Tunneling Microscope Images of Graphite. *Appl. Phys. Lett.* **1990**, *56*, 2396–2404.
3. Warner, J. H.; Rümmeli, M. H.; Gemming, T.; Büchner, B.; Briggs, G. A. D. Direct Imaging of Rotational Stacking Faults in Few Layer Graphene. *Nano Lett.* **2009**, *9*, 102–106.
4. Chen, B.; Lu, K. Moiré Pattern Nanopore and Nanorod Arrays by Focused Ion Beam Guided Anodization and Nanoimprint Molding. *Langmuir* **2011**, *27*, 4117–4125.
5. Luchnikov, V.; Kondyurin, A.; Formanek, P.; Lichte, H.; Stamm, M. Moiré Patterns in Superimposed Nanoporous Thin Films Derived from Block-Copolymer Assemblies. *Nano Lett.* **2007**, *7*, 3628–3632.
6. Albrecht, T. R.; Mizes, H. A.; Mizes, J.; Nogami, J.; Park, S.; Quate, C. F. Observation of Tilt Boundaries in Graphite by Scanning Tunneling Microscopy and Associated Multiple Tip Effects. *Appl. Phys. Lett.* **1988**, *52*, 362–364.
7. Wong, H. S.; Durkan, C. Unraveling the Rotational Disorder of Graphene Layers in Graphite. *Phys. Rev. B* **2010**, *81*, 045403.
8. Sun, Z.; Hamalainen, S. K.; Sainio, J.; Lahtinen, J.; Vanmaekelbergh, D.; Liljeroth, P. Topographic and Electronic Contrast of the Graphene Moiré on Ir(111) Probed by Scanning Tunneling Microscopy and Noncontact Atomic Force Microscopy. *Phys. Rev. B* **2011**, *83*, 081415(R).
9. Glaubert, A. M. Moiré Patterns in Electron Micrographs of a Bacterial Membrane. *J. Cell. Sci.* **1966**, *1*, 425–428.
10. Talapin, D. V.; Shevchenko, E. V.; Bodnarchuk, M. I.; Ye, X.; Chen, J.; Murray, C. B. Quasicrystalline Order in Self-Assembled Binary Nanoparticle Superlattices. *Nature* **2009**, *461*, 964–967.
11. Shevchenko, E. V.; Talapin, D. V.; Kotov, N. A.; O'Brien, S.; Murray, C. B. Structural Diversity in Binary Nanoparticle Superlattices. *Nature* **2006**, *439*, 55–59.
12. Dong, A. G.; Chen, J.; Vora, P. M.; Kikkawa, J. M.; Murray, C. B. Binary Nanocrystal Superlattice Membranes Self-Assembled at the Liquid-Air Interface. *Nature* **2010**, *466*, 474–477.
13. Shevchenko, E. V.; Kortright, J. B.; Talapin, D. V.; Aloni, S.; Alivisatos, A. P. Quasi-Ternary Nanoparticle Superlattices Through Nanoparticle Design. *Adv. Mater.* **2007**, *19*, 4183–4188.
14. Dong, A.; Ye, X.; Chen, J.; Murray, C. B. Two-Dimensional Binary and Ternary Nanocrystal Superlattices: The Case of Monolayers and Bilayers. *Nano Lett.* **2011**, *11*, 1804–1809.
15. Dong, A.; Chen, J.; Oh, S. J.; Koh, W.; Xiu, F.; Ye, X.; Ko, D.; Wang, K. L.; Kagan, C. R.; Murray, C. B. Multiscale Periodic Assembly of Striped Nanocrystal Superlattice Films on a Liquid Surface. *Nano Lett.* **2011**, *11*, 841–846.
16. Evers, W. H.; Friedrich, H.; Filion, L.; Dijkstra, M.; Vanmaekelbergh, D. Observation of a Ternary Nanocrystal Superlattice and Its Structural Characterization by Electron Tomography. *Angew. Chem., Int. Ed.* **2009**, *48*, 9655–9657.
17. Lee, S. Y.; Gradon, L.; Janeczko, S.; Iskandar, F.; Okuyama, K. Formation of Highly Ordered Nanostructures by Drying Micrometer Colloidal Droplets. *ACS Nano* **2010**, *4*, 4717–4724.
18. Talapin, D. V.; Lee, J. S.; Kovalenko, M. V.; Shevchenko, E. V. Prospects of Colloidal Nanocrystals for Electronic and Optoelectronic Applications. *Chem. Rev.* **2010**, *110*, 389–458.
19. Wen, T.; Majetich, S. A. Ultra-Large-Area Self-Assembled Monolayers of Nanoparticles. *ACS Nano* **2011**, *5*, 8868–8876.
20. Dong, A.; Chen, J.; Ye, X.; Kikkawa, J. M.; Murray, C. B. Enhanced Thermal Stability and Magnetic Properties in NaCl-Type FePt–MnO Binary Nanocrystal Superlattices. *J. Am. Chem. Soc.* **2011**, *133*, 13296–13299.
21. Lee, J.-S.; Bodnarchuk, M. I.; Shevchenko, E. V.; Talapin, D. V. “Magnet-in-the-Semiconductor” FePt-PbS and FePt-PbSe Nanostructures: Magnetic Properties, Charge Transport, and Magnetoresistance. *J. Am. Chem. Soc.* **2010**, *132*, 6382–6391.
22. Quan, Z. W.; Fang, J. Y. Superlattices with Non-Spherical Building Blocks. *Nano Today* **2010**, *5*, 390–411.
23. Nie, Z. H.; Petukhova, A.; Kumacheva, E. Properties and Emerging Applications of Self-Assembled Structures Made from Inorganic Nanoparticles. *Nat. Nanotechnol.* **2010**, *5*, 15–25.
24. Peng, Z. A.; Peng, X. G. Formation of High-Quality CdTe, CdSe, and CdS Nanocrystals Using CdO as Precursor. *J. Am. Chem. Soc.* **2001**, *123*, 183–184.
25. Gur, I.; Fromer, N. A.; Geier, M. L.; Alivisatos, A. P. Air-Stable All-Inorganic Nanocrystal Solar Cells Processed from Solution. *Science* **2005**, *310*, 462–465.
26. Manna, L.; Milliron, D. J.; Meisel, A.; Scher, E. C.; Alivisatos, A. P. Controlled Growth of Tetrapod-Branched Inorganic Nanocrystals. *Nat. Mater.* **2003**, *2*, 382–385.
27. Liu, K.; Zhao, N. N.; Kumacheva, E. Self-Assembly of Inorganic Nanorods. *Chem. Soc. Rev.* **2010**, *40*, 656–671.
28. Ryan, K. M.; Mastrianni, A.; Stancil, K. A.; Liu, H. T.; Alivisatos, A. P. Electric-Field-Assisted Assembly of Perpendicularly Oriented Nanorod Superlattices. *Nano Lett.* **2006**, *6*, 1479–1482.
29. Carbone, L.; Nobile, C.; De Giorgi, M.; Della Sala, F.; Morello, G.; Pompa, P.; Hytch, M.; Snoeck, E.; Fiore, A.; Franchini, I. R.; et al. Synthesis and Micrometer-Scale Assembly of Colloidal CdSe/CdS Nanorods Prepared by a Seeded Growth Approach. *Nano Lett.* **2007**, *7*, 2942–2950.
30. Ahmed, S.; Ryan, K. M. Centimetre Scale Assembly of Vertically Aligned and Close Packed Semiconductor Nanorods from Solution. *Chem. Commun.* **2009**, 6421–6423.
31. Kelly, D.; Singh, A.; Barrett, C. A.; O'Sullivan, C.; Coughlan, C.; Laffir, F. R.; O'Dwyer, C.; Ryan, K. M. A Facile Spin-Cast Route for Cation Exchange of Multilayer Perpendicularly-Aligned Nanorod Assemblies. *Nanoscale* **2011**, *3*, 4580–4583.
32. Ahmed, S.; Ryan, K. M. Self-Assembly of Vertically Aligned Nanorod Supercrystals Using Highly Oriented Pyrolytic Graphite. *Nano Lett.* **2007**, *7*, 2480–2485.
33. Kang, C. C.; Lai, C. W.; Peng, H. C.; Shyu, J. J.; Chou, P. T. 2D Self-Bundled CdS Nanorods with Micrometer Dimension in the Absence of an External Directing Process. *ACS Nano* **2008**, *2*, 750–756.
34. Singh, A.; Gunning, R. D.; Sanyal, A.; Ryan, K. M. Directing Semiconductor Nanorod Assembly into 1D or 2D Supercrystals by Altering the Surface Charge. *Chem. Commun.* **2010**, *46*, 7193–7195.
35. Singh, A.; Gunning, R. D.; Ahmed, S.; Barrett, C. A.; English, N. J.; Garate, J.-A.; Ryan, K. M. Controlled Semiconductor Nanorod Assembly from Solution: Influence of Concentration, Charge and Solvent Nature. *J. Mater. Chem.* **2012**, *22*, 1562–1569.
36. Baranov, D.; Fiore, A.; van Huis, M.; Giannini, C.; Falqui, A.; Lafont, U.; Zandbergen, H.; Zanella, M.; Cingolani, R.; Manna, L. Assembly of Colloidal Semiconductor Nanorods in Solution by Depletion Attraction. *Nano Lett.* **2010**, *10*, 743–749.
37. Baker, J. L.; Widmer-Cooper, A.; Toney, M. F.; Geissler, P. L.; Alivisatos, A. P. Device-Scale Perpendicular Alignment of Colloidal Nanorods. *Nano Lett.* **2010**, *10*, 195–201.
38. Zanella, M.; Gomes, R.; Povia, M.; Giannini, C.; Zhang, Y.; Riskin, A.; van Bael, M.; Hens, Z.; Manna, L. Self-Assembled Multilayers of Vertically Aligned Semiconductor Nanorods on Device-Scale Areas. *Adv. Mater.* **2011**, *23*, 2205–2209.
39. Rivest, J. B.; Swisher, S. L.; Fong, L.-K.; Zheng, H.; Alivisatos, A. P. Assembled Monolayer Nanorod Heterojunctions. *ACS Nano* **2011**, *5*, 3811–3816.
40. Singh, A.; Geaney, H.; Laffir, F.; Ryan, K. M. Colloidal Synthesis of Wurtzite Cu<sub>2</sub>ZnSnS<sub>4</sub> Nanorods and Their Perpendicular Assembly. *J. Am. Chem. Soc.* **2012**, *134*, 2910–2913.
41. Hu, J.; Li, L.-S.; Yang, W.; Manna, L.; Wang, L.-W.; Alivisatos, A. P. Linearly Polarized Emission from Colloidal Semiconductor Quantum Rods. *Science* **2001**, *292*, 2060–2063.
42. Gonzalez-Valls, I.; Lira-Cantu, M. Vertically-Aligned Nanostructures of ZnO for Excitonic Solar Cells: a Review. *Energy Environ. Sci.* **2009**, *2*, 19–34.
43. Amirav, L.; Alivisatos, A. P. Photocatalytic Hydrogen Production with Tunable Nanorod Heterostructures. *J. Phys. Chem. Lett.* **2011**, *1*, 1051–1054.

44. Krahne, R.; Morello, G.; Figuerola, A.; George, C.; Deka, S.; Manna, L. Physical Properties of Elongated Inorganic Nanoparticles. *Phys. Rep.* **2011**, *501*, 75–221.
45. Li, L.-S.; Alivisatos, A. P. Origin and Scaling of the Permanent Dipole Moment in CdSe Nanorods. *Phy. Rev. Lett.* **2003**, *90*, 097402.
46. Nann, T.; Schneider, J. Origin of Permanent Electric Dipole Moments in Wurtzite Nanocrystals. *J. Chem. Phys. Lett.* **2004**, *384*, 150–152.